ISSN 1674-1056
http://cpb.iphy.ac.cn
http://iopscience.iop.org/cpb
中国物理 B
Chinese Physics
中国物理 Chinese Physics B

# Dual-polarized lens antenna based on multimode metasurfaces

Hao-Fang Wang(王浩放), Zheng-bin Wang(王正斌), Yong Cheng(程勇), Ye-Rong Zhang(张业荣)

**Citation:**Chin. Phys. B . 2018, 27(11): 118401. **doi:** 10.1088/1674-1056/27/118401
Journal homepage: http://cpb.iphy.ac.cn; http://iopscience.iop.org/cpb

**What follows is a list of articles you may be interested in**

---

## Correction of failure in antenna array using matrix pencil technique

S U Khan, M K A Rahim

Chin. Phys. B . 2017, 26(6): 068401. **doi:** 10.1088/1674-1056/26/6/068401

## An ultra-wideband pattern reconfigurable antenna based on graphene coating

YanNan Jiang(姜彦南), Rui Yuan(袁锐), Xi Gao(高喜), Jiao Wang(王娇), SiMin Li(李思敏), Yi-Yu Lin(林诒玉)

Chin. Phys. B . 2016, 25(11): 118402. **doi:** 10.1088/1674-1056/25/11/118402

## Metallic spherical anechoic chamber for antenna pattern measurement

Ali Farahbakhsh, Mohammad Khalaj-Amirhosseini

Chin. Phys. B . 2016, 25(8): 088401. **doi:** 10.1088/1674-1056/25/8/088401

## Dual-band LTCC antenna based on $0.95Zn_2SiO_4$-$0.05CaTiO_3$ ceramics for GPS/UMTS applications

Dou Gang, Li Yu-Xia, Guo Mei

Chin. Phys. B . 2015, 24(10): 108401. **doi:** 10.1088/1674-1056/24/10/108401

## Four-dimensional parameter estimation of plane waves using swarming intelligence

Fawad Zaman, Ijaz Mansoor Qureshi, Fahad Munir, Zafar Ullah Khan

Chin. Phys. B . 2014, 23(7): 078402. **doi:** 10.1088/1674-1056/23/7/078402

---

# Dual-polarized lens antenna based on multimode metasurfaces*

Hao-Fang Wang(王浩放)[1,2], Zheng-Bin Wang(王正斌)[1,2,†], Yong Cheng(程勇)[1], and Ye-Rong Zhang(张业荣)[1,‡]

[1] College of Electronic and Optical Engineering, Nanjing University of Posts and Telecommunications, Nanjing 210023, China
[2] State Key Laboratory of Millimeter waves, Nanjing 210096, China

(Received 17 July 2018; revised manuscript received 23 August 2018; published online 19 October 2018)

We propose a dual-polarized lens antenna system based on isotropic metasurfaces for 12 GHz applications. The metasurface lens is composed of subwavelength unit cells ($0.24\lambda_0$) with metallic strips etched on the top and bottom sides of the unit cell, and a cross-slots metallic layer in the middle that serves as the ground. The multimode resonance in the unit cell can realize a large phase shift (covering 0°–360°), and the total transmission efficiency of the lens is above 80%. The feed antenna at the focal point of the lens is a broadband dual-polarized microstrip antenna. Both the simulated and the measured results demonstrate that the dual-polarized lens antenna system can realize a gain of more than 16.1 dB, and an input port isolation of more than 25.0 dB.

**Keywords:** dual polarization, metasurfaces, lens antenna, multimode resonance, low-profile

**PACS:** 84.40.Ba, 41.20.Jb **DOI:** 10.1088/1674-1056/27/11/118401

## 1. Introduction

Dual-polarized antennas can increase the capacity and reliability of wireless communication links, and have been widely used in multiple-input multiple-output (MIMO) systems, radars,[1] and satellite communication systems. While metasurfaces have been widely used to control the electromagnetic field distribution and electromagnetic wave propagation.[2] Due to the benefits of low profile, low cost, and light weight, many reported metasurfaces have been used in lens antenna designs.[3–5] Therefore, we are motivated to design a dual-polarized lens antenna based on metasurfaces. Due to the electromagnetic characteristic of the unit cell, metasurfaces composed of anisotropic unit cells are polarization dependent,[6,7] which would be problematic for dual polarization applications. Thus, metasurfaces composed of isotropic unit cells are more promising. Isotropic metasurfaces can be further classified as combination-type[5,8–10] and single-type.[3,4,11] For combination-type metasurface lens, many different unit cells are required, which severely increase the design complexity.[9,12] In addition, one-layer combination-type metasurfaces have an upper limit of transmission efficiency,[13] which makes it almost impossible to design dual polarized lens antennas with high isolation. For single-type two-layer isotropic metasurfaces, it can realize isotropic, large phase shift, and high transmission efficiency, which meets the requirements for dual polarized lens antennas.

In this work, we propose a single-type isotropic metasurface lens, which is composed of 0.24 wavelength unit cells with metallic strips etched on the top and bottom sides of the unit cell, and a cross-slot metallic layer in the middle that serves as the ground. Through tuning the strip-line length, the unit cell can operate in different modes. Each unit cell can realize a large phase shift (covering 0°– 360°), and the whole lens can realize a high transmission efficiency (> 80%). Then, a dual polarized patch antenna is located at the focal point of the lens as the primary feed to form a low-profile lens antenna system. The full-wave simulation results demonstrate that the dual-polarized lens antenna exhibits a high port isolation (> 25.0 dB) and high gain (> 16.1 dB).

## 2. Unit cell design and operation principles

The geometry of the proposed subwavelength unit cell of the metasurface is shown in Fig. 1(a). There are two layers of dielectric substrates (AD255C) with the relative permittivity $\varepsilon_r = 2.55$ and the thickness $h/2 = 2$ mm. The total thickness and width of the unit cell are $h = 4$ mm ($0.16\lambda_0$, where $\lambda_0$ is the wavelength at the center frequency of 12 GHz) and $L = 6$ mm ($0.24\lambda_0$), respectively. Four metallic strips are etched symmetrically on the top and bottom sides. The width of the small strip is $p_w$, and the slot width between these strips is $p_s$. The middle metallic layer is the ground with cross H slots. The other detailed geometric parameters of the unit cell are $p_l = 2$ mm, $p_s = 0.2$ mm, $p_w = 0.3$ mm, $s_l = 5.55$ mm, $s_w = 0.2$ mm, $g_1 = 0.8$ mm, and $g_2 = 1.1$ mm. Figure 2 shows the simulated transmission properties of the unit cell, where periodic boundary conditions are imposed in the $x$- and $y$-direction (Fig. 1(b)). The transmission magnitude (the solid

*Project supported by the Open Research Program of the State Key Laboratory of Millimeter Waves, China (Grant No. K201926), the Postgraduate Research & Practice Innovation Program of Jiangsu Province, China, and the Nanjing University of Posts and Telecommunications Scientific Foundation, China (Grant No. NY215137).

†Corresponding author. E-mail: wangzb@njupt.edu.cn
‡Corresponding author. E-mail: zhangyr@njupt.edu.cn

© 2018 Chinese Physical Society and IOP Publishing Ltd 

line in Fig. 2) shows three poles at the frequencies of 9 GHz, 12 GHz, and 14.5 GHz, which are marked as mode 1, mode 2, and mode 3, respectively.

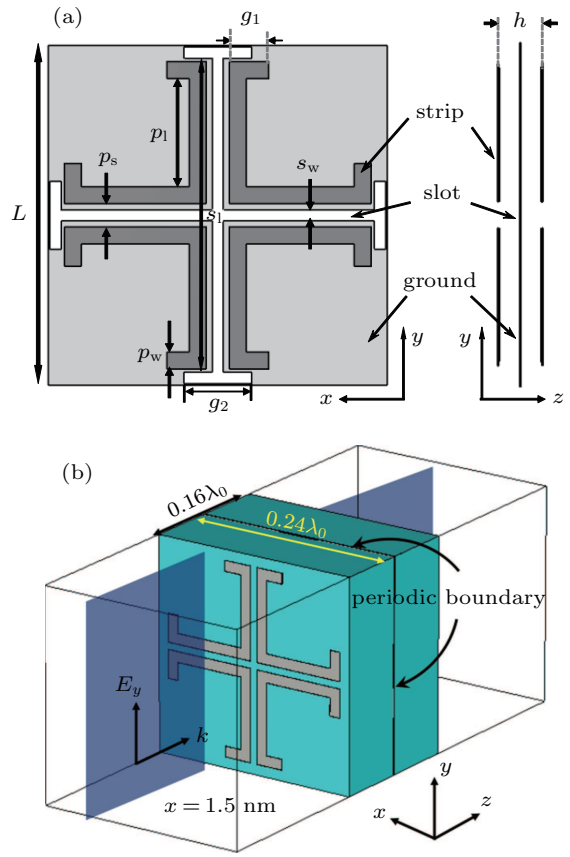



**Fig. 1.** (color online) (a) Geometry of the proposed unit cell and (b) simulation model.

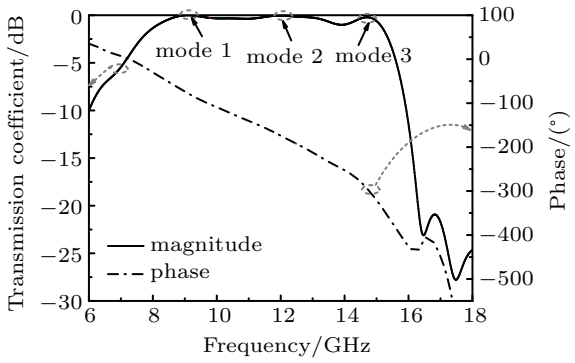



**Fig. 2.** Simulated transmission properties of a unit cell with the given geometries.

To reveal the physical mechanisms of the unit cell at different modes, the $E$-field distribution at 12 GHz is analyzed, and the results are shown in Fig. 3. Figures 3(a)–3(d) show the electric field distribution of mode 1 on the plane perpendicular to the $x$ axis ($x = 1.5$ mm). From the figure, we can see that $E_z$ between the strip and the ground is $TM_{10}$ mode, which is mirror symmetric with respect to the ground. Component $E_y$ along the strip and slot gap is excited as shown in Fig. 3(d). Due to the two symmetric $TM_{10}$ modes, the incident electric field is coupled to the transmitted field almost without any change, which indicates that mode 1 does not bring any phase change to $E_y$. Figure 3(b) shows the top view of the structure, where $g_1 = g_2 = 0$. Figure 3(c) shows the equivalent transmission field of the unit cell operated in mode 1.

Figure 3(e) shows the electric field distribution of mode 2 on the plane perpendicular to the $x$ axis ($x = 1.5$ mm). From Fig. 3(h), we can see that between the upper and lower strips, $E_z$ has three resonant parts; i.e., the antiphase $TM_{20}$ mode[14] near upper and lower strips and the weak $TM_{10}$ mode near the ground. From Figs. 3(e) and 3(h), we can see that the three resonant parts lead to 180° phase shift toward the transmitted electric field with respect to the incident electric field. Figure 3(f) shows the top view of the structure, where $g_1 = 0.8$ mm and $g_2 = 1.1$ mm. Figure 3(g) shows the equivalent transmission field $E_y$ of the unit cell operated in mode 2.

Figure 3(i) shows the electric field distribution of mode 3 on the plane perpendicular to the $x$ axis ($x = 1.5$ mm). From Fig. 3(l), we can see that between the strips and the ground, $E_z$ is a combination mode of strong resonance $TM_{10}$ and $TM_{20}$, and they are mirror symmetric with respect to the ground. Due to the mirror symmetric resonance modes, the incident electric field is coupled to the transmitted field with 360° phase shift. Figure 3(j) shows the top view of the structure, where $g_1 = 1.8$ mm and $g_2 = 3.5$ mm. Figure 3(k) shows the equivalent transmission $E$ field of the unit cell operated in mode 3.

To further clarify the resonant mechanism, the surface current distributions at 12 GHz are analyzed. Figures 4(a)–4(c) show the surface currents in the upper strips, the metal ground, and the lower strips at modes 1, 2, and 3, respectively. Figure 4(a) shows that the surface currents in the upper and lower strips are very weak, while the current along the gap in the ground is very strong. This phenomenon is consistent with the scenario in Figs. 3(a) –3(d), where the electric field in mode 1 produces $TM_{10}$ mode near the ground. From Fig. 4(a), we can see that the currents in the upper and lower strips are in the same direction, which further demonstrates that mode 1 does not introduce phase change into $E_y$. Figure 4(b) shows that the currents in the upper and lower strips are stronger than that on the ground, which is consistent with the strong $TM_{20}$ mode near the upper and lower strips and the weak $TM_{10}$ mode near the ground. Meanwhile, the phase inversion of the surface current in the upper and lower strips is coincident with the electric field distribution in Figs. 3(e)–3(h). Figure 4(c) shows strong surface currents in the three metal layers. The phases of the surface currents in the upper strips are opposite to that in the metal ground, and the phases of the surface currents in the metal ground and lower strips are also opposite to each other. Therefore, mode 3 can achieve 360° phase change, which is consistent with that in Figs. 3(i)–3(l).

Through tuning the strip length ($g_1$) and the slot length ($g_2$), the unit will operate at the same frequency in different

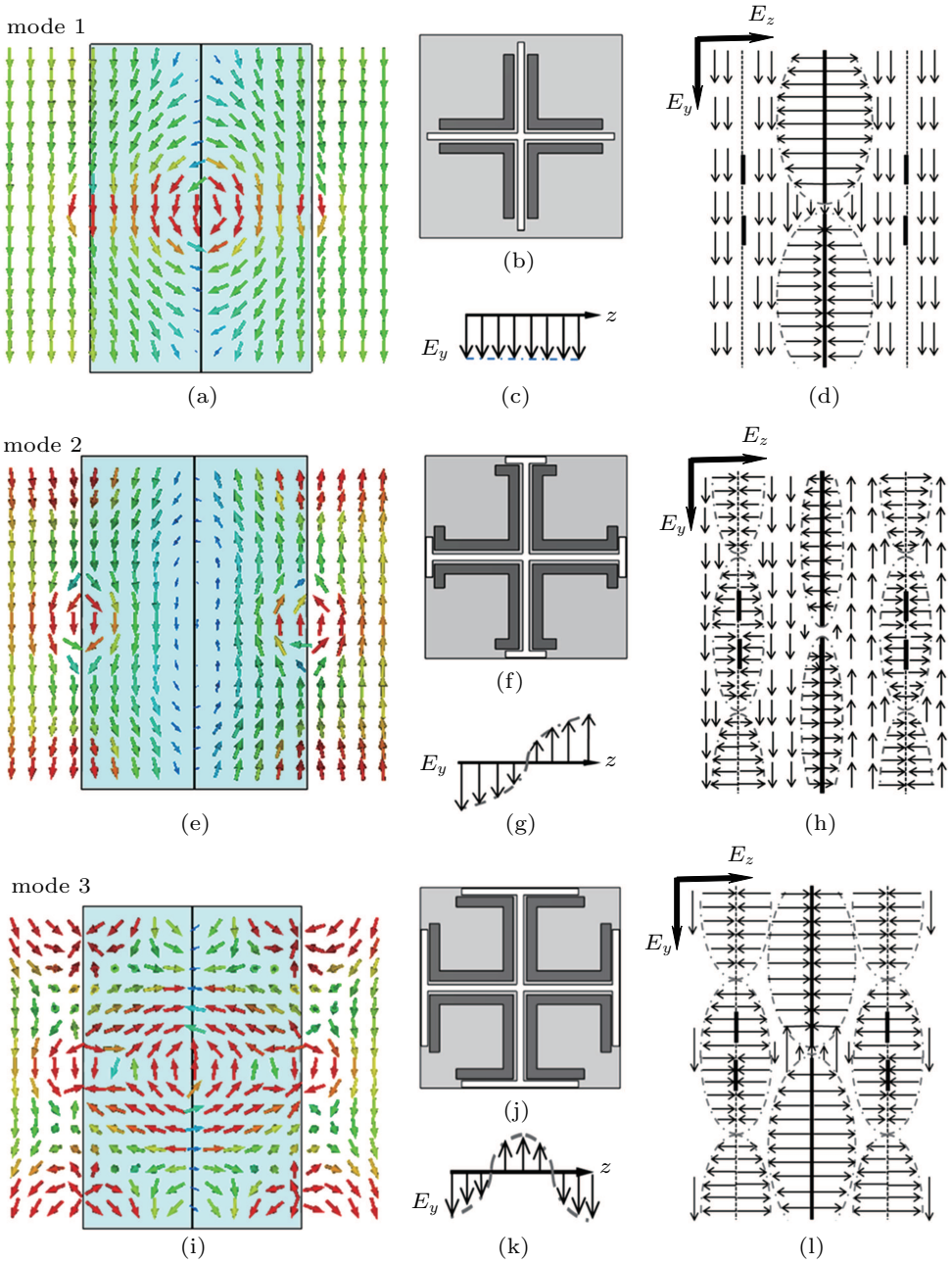



**Fig. 3.** (color online) Mode 1: (a) simulated $E$ field distribution on $x = 1.5$ mm plane, (b) geometry of unit cell operating in mode 1, (c) equivalent transmission $E$ field of the unit, and (d) sketch of the operation mechanism. Mode 2: (e) simulated $E$ field distribution on $x = 1.5$ mm plane, (f) geometry of unit cells operating in mode 2, (g) equivalent transmission $E$ field of the unit, and (h) sketch of the operation mechanism. Mode 3: (i) simulated $E$ field distribution on $x = 1.5$ mm plane, (j) geometry of unit cells operating in mode 3, (k) equivalent transmission $E$ field of the unit, and (l) sketch of the operation mechanism.

modes, which in turn can realize the required phase coverage and high transmission efficiency. Figure 5 shows the transmission properties of three unit cells that can realize full phase coverage and satisfactory transmission efficiency at 12 GHz. The detailed dimensions of the three unit cells are shown in Table 1, which can be expressed as a parameter vector $\boldsymbol{G}_m = (g_1(m), g_2(m))$.

Through the piecewise spline interpolation of the parameter vectors, we can obtain the equation of relation between the parameter vector and the mode $m$,

$$\boldsymbol{G}_m = \begin{cases} \boldsymbol{G}_1 + (\boldsymbol{G}_2 - \boldsymbol{G}_1)(m-1), & 1 \le m \le 2, \\ \boldsymbol{G}_2 + (\boldsymbol{G}_3 - \boldsymbol{G}_2)(m-2), & 2 < m \le 4. \end{cases} \quad (1)$$

Figure 6 shows the relations between the transmission property and the operation mode $m$ of the subwavelength unit cells. From the figure, we can see that the varying of the operation mode leads to the full phase coverage, and the transmission efficiency is satisfactory from 11.0 GHz to 13.0 GHz, which can be used to design the planar lens antenna system.

**Table 1.** Dimensions of three unit cells operated at modes 1, 2, and 3, respectively.

| $\boldsymbol{G}_m$ | $g_1$/mm | $g_2$/mm |
|---|---|---|
| $\boldsymbol{G}_1$ (mode 1) | 0 | 0 |
| $\boldsymbol{G}_2$ (mode 2) | 0.8 | 1.1 |
| $\boldsymbol{G}_3$ (mode 3) | 1.8 | 3.5 |

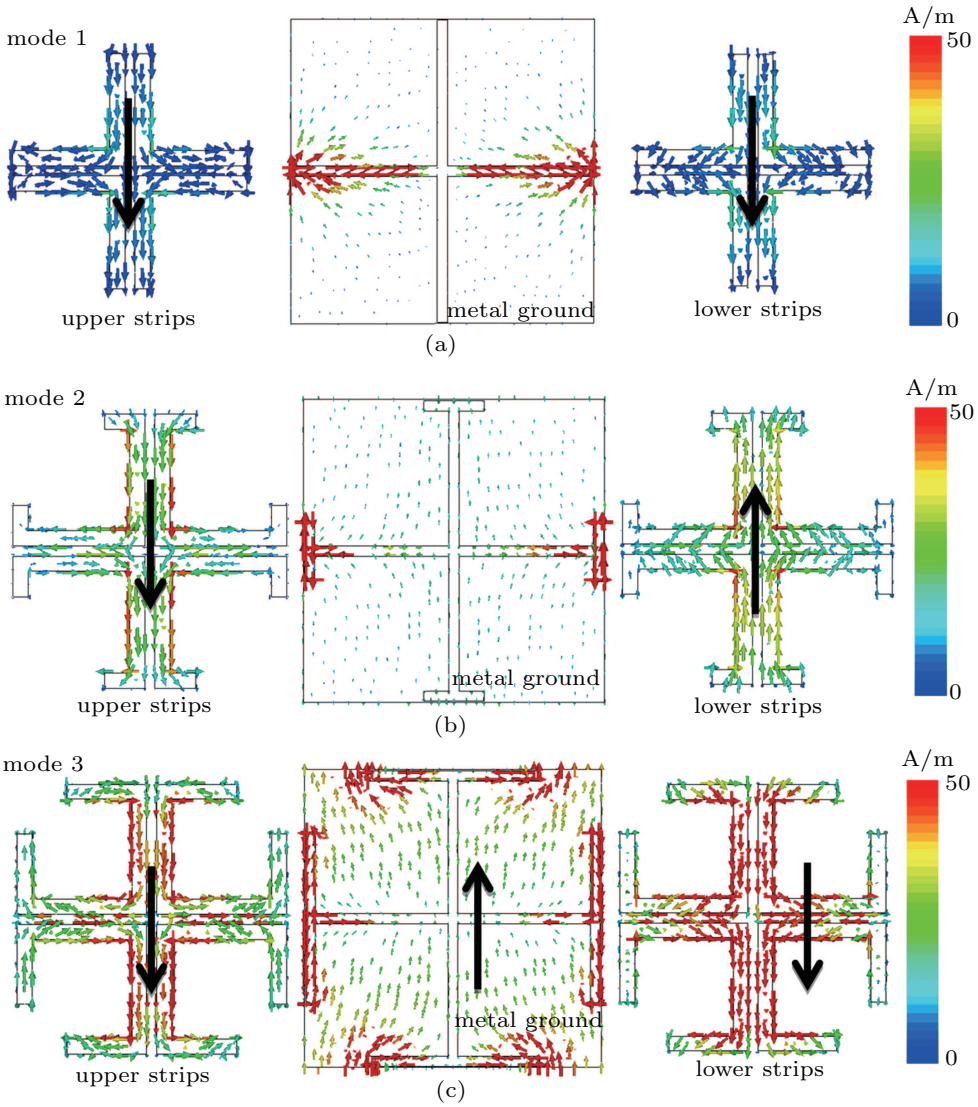



**Fig. 4.** (color online) Surface current distribution in the upper strips, the metal ground, and the lower strips in (a) mode 1, (b) mode 2, and (c) mode 3.

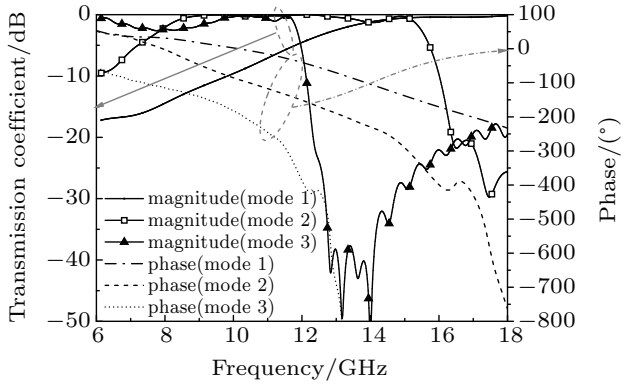



**Fig. 5.** Simulated transmission properties of three unit cells at 12 GHz.

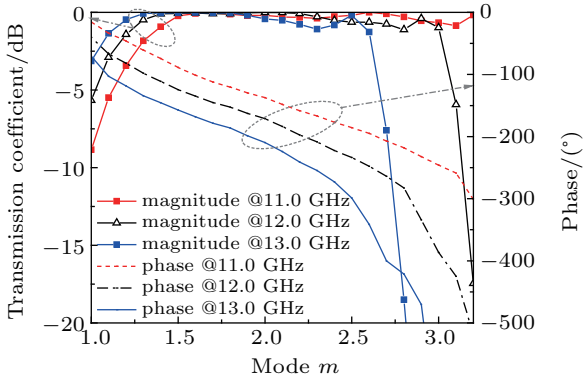



**Fig. 6.** (color online) Simulated transmission properties vs. mode $m$ at 11.0 GHz, 12.0 GHz, and 13.0 GHz.

## 3. Lens design

Based on these subwavelength unit cells, an isotropic lens that mimics the transmission phase profile of a double-convex dielectric lens is fabricated. According to the equal optical path principle,[15] the phase distribution at the radial direction should be written as

$$\phi(r) = 2n\pi + k_0(\sqrt{r^2+F^2} - F), \tag{2}$$

where $n$ is an arbitrary integer, $k_0$ is the free space wavenumber at the operating frequency, and $F$ and $r$ are the focal length and the radial distance, respectively. In our design, the lens is

composed of $16 \times 16$ spatial phase shifters with dimensions of $0.24\lambda_0 \times 0.24\lambda_0$. The focal length of the lens is designed to be $F = 28$ mm ($1.17\lambda_0$), resulting in an $F/D$ (focal length $F$ over diameter $D$) ratio of 0.30. According to the phase distribution calculated from Eq. (2), we can obtain the required mode $m$ of the unit cell from Fig. 6. Figure 7(a) displays the spatial distribution of the required mode $m$, and figure 7(b) shows the fabricated metasurface lens.

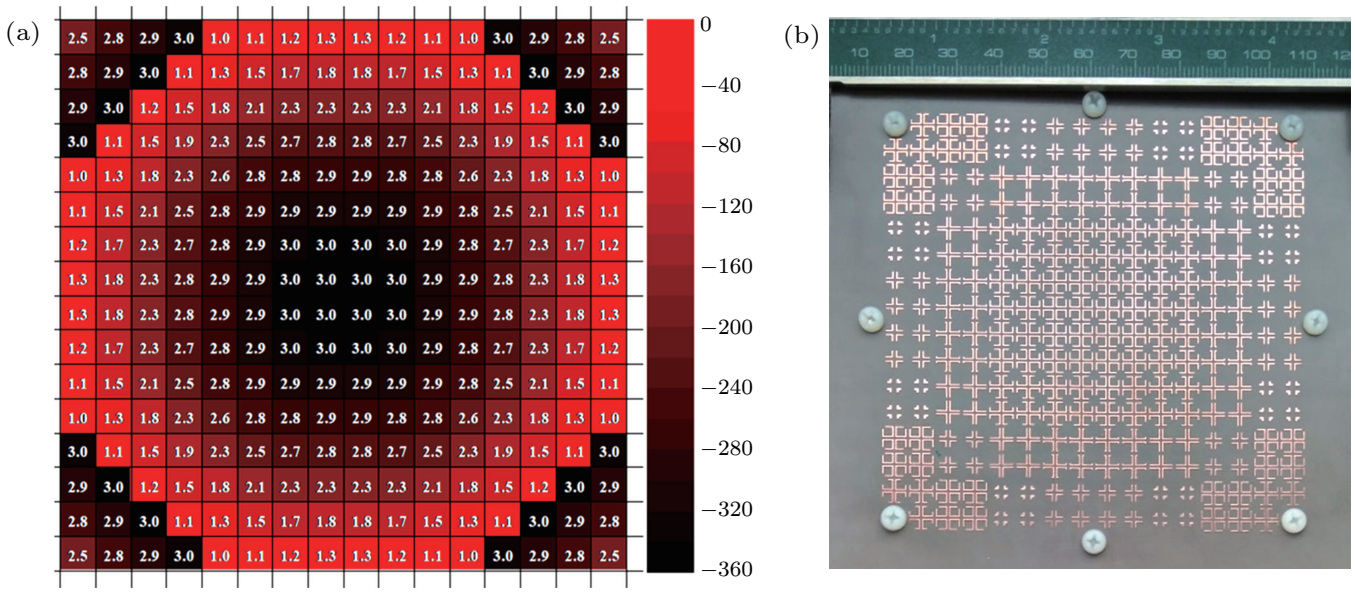



**Fig. 7.** (color online) (a) Spatial distribution of the required phase and the mode $m$ of the lens, and (b) the fabricated planar lens.

The total transmission efficiency of the lens should be the sum of the weighted element transmission coefficients,[16] and is expressed as

$$\text{Trans. coeff.} = \frac{\sum_m \sum_n [E(m,n)|T(m,n)|]^2}{\sum_m \sum_n [E(m,n)]^2}, \tag{3}$$

where $E(m,n)$ and $T(m,n)$ are the incident electric field and the transmission coefficient of the $m,n$-th element, respectively. For this design, the maximum transmission efficiency can reach 80%.

## 4. Lens antenna design and the measured results

The lens antenna system is composed of a metasurface lens and a dual-polarized patch antenna. The phase center of the patch antenna is located at the focal point of the planar lens. Figure 8(a) shows the simulated and measured isolations between the two orthogonal ports with and without the lens. The inset shows the simulation model of the lens antenna system in the full-wave simulation platform Altair FEKO.[17] From the figure, we can see that the isolation is less than −25 dB in a wide frequency band, which means that the dual-polarized antenna system can operate very well. Figures 8(b) and 8(c) show the plots of simulated and measured return loss versus frequency of the feed port 1 and feed port 2 with/without the surface lens, respectively. The two figures demonstrate good consistency between the simulated results and the measured results. They also show that the −10 dB bandwidth of the antenna system ranges from 11.0 GHz to 13.5 GHz, and the mutual coupling between the feed antenna and the metasurface lens can be neglected.

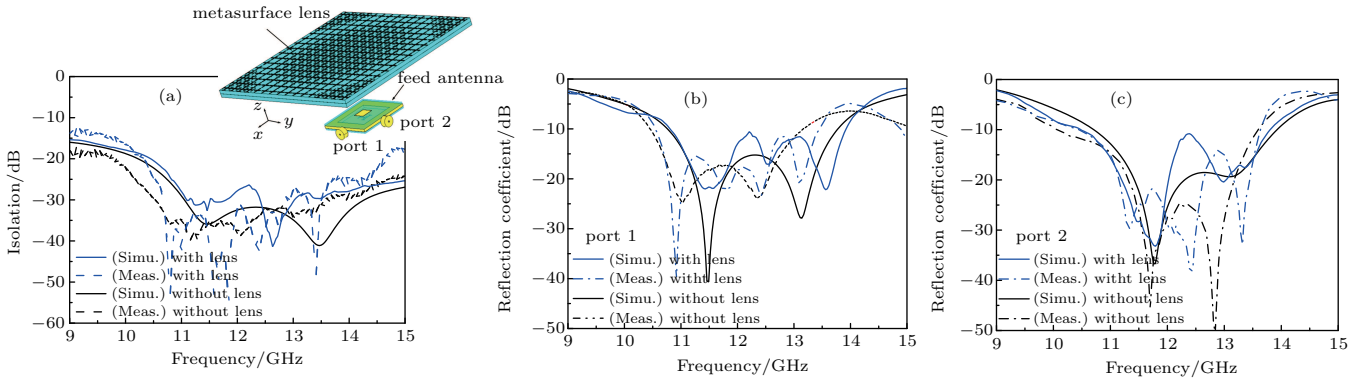



**Fig. 8.** (color online) (a) Plots of frequency-dependent simulated and measured isolation between port 1 and port 2 with/without loading the lens. Plots of frequency-dependent simulated and measured reflection coefficient of (b) port 1 and (c) port 2 with and without loading the lens.

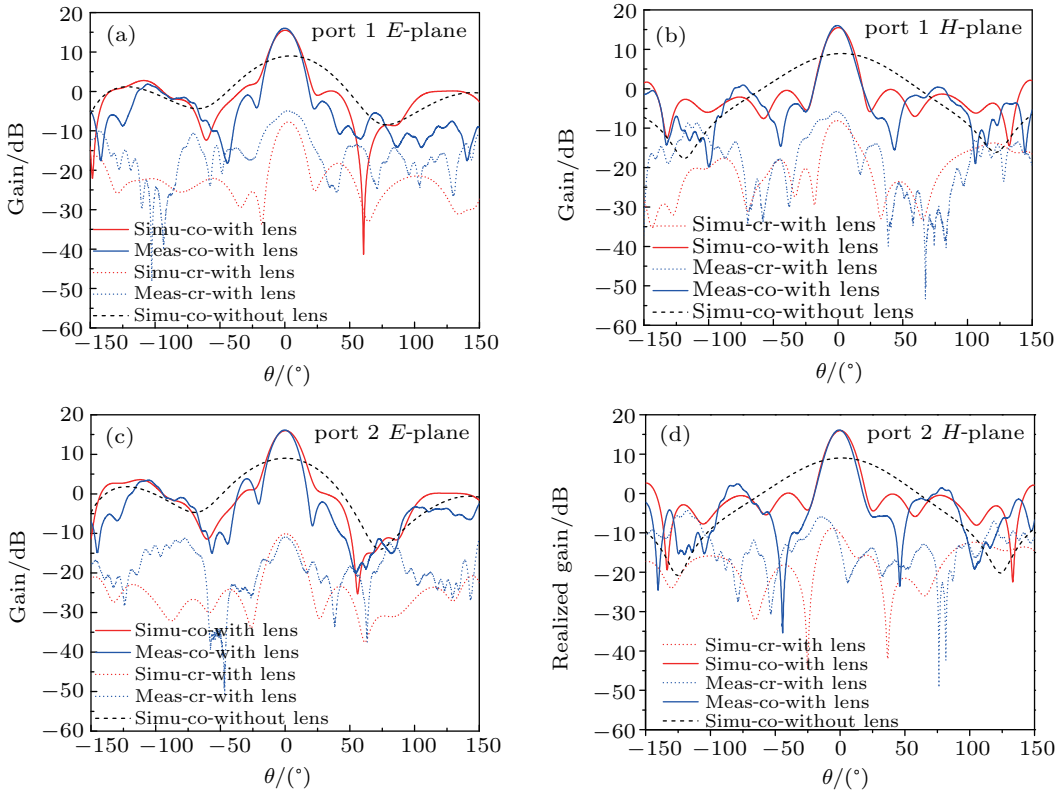



**Fig. 9.** (color online) Plots of $\theta$-dependent simulated and measured radiation patterns at 12.0 GHz (a) in $E$-plane and (b) in $H$-plane fed by port 1. The radiation patterns fed by port 2 (c) in $E$-plane and (d) in $H$-plane.

Then, the radiation pattern of the fabricated low-profile lens antenna is tested in our microwave anechoic chamber. Figure 9 shows the simulated and measured co- and cross-polarization patterns at a center frequency of 12.0 GHz. From the figure, we can see that the bore-side gain of the lens antenna is about 16.1 dB, which is enhanced by about 7.2 dB with respect to the feed patch antenna. The co- and cross-polar radiation patterns demonstrate that the dual-polarized antenna system has very good performance in cross-polarization isolation ($< -25$ dB) and impedance matching. Nevertheless, the side lobe level (SSL) is about $-13$ dB, which is unsatisfactory. In the next step, we will optimize the feed antenna and the metasurface lens to improve the radiation performance.

Figure 10 further shows the simulated and measured peak gains fed by ports 1 and 2, respectively. From the figure, we can see that the 1-dB gain bandwidth achieved by this lens antenna is 1 GHz (8.3% of the center frequency). Compared with the simulated results, the measured peak gains are slightly shift toward high frequency band, which should be due to the fabrication tolerance and the alignment tolerance. Nevertheless, compared with the earlier designs shown in Table 2, this dual-polarized lens antenna has low profile, broad gain bandwidth, and excellent port isolation.

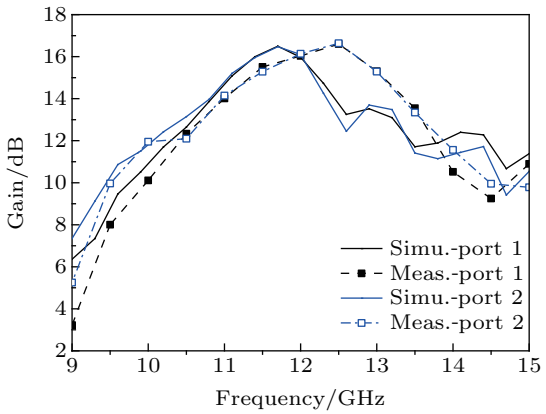



**Fig. 10.** (color online) Plots of simulated and measured peak gain versus frequency fed by ports 1 and 2, respectively.

**Table 2.** Comparison of lens antennas between this work and previous work.

| Ref. | Frequency/GHz | Antenna system | Dual/single polarization | Aperture efficiency/% | Focal length $\lambda_0$ | 1-dB gain BW/% |
|---|---|---|---|---|---|---|
| [4] | 9.7 | yes | single | 41 | 2.77 | 5.7 |
| [12] | 10 | yes | single | 30 | 1 | <3 |
| [18] | 10 | no | dual | 27.5 | 7.17 | <10 |
| [19] | 10 | no | single | 36 | 6.72 | 3.5 |
| [20] | 13 | yes | circular | 41 | 1.1 | 3.5 |
| This work | 12 | yes | Dual | 25 | 1.17 | 8.3 |

## 5. Conclusions

We present a low-profile, dual-polarized lens antenna system that is based on multimode resonant metasurfaces. The total size of the metasurface lens is 92 mm×92 mm ($3.84\lambda_0 \times 3.84\lambda_0$), and the $F/D$ of the lens is 0.30. The maximum transmission efficiency is above 80% over the operating band (11–13 GHz). The measured results demonstrate that the isolation of the dual-polarized lens antenna is more than 25 dB, and the gain is more than 16.1 dB. The maximum 1-dB gain bandwidth and the aperture efficiency of the lens antenna are 8.3% and 25%, respectively.

## References


[1] Mishra P K, Jahagirdar D R and Kumar G 2015 *IEEE Antennas & Propag. Mag.* **56** 238

[2] Gagnon N, Petosa A and McNamara D A 2013 *IEEE Antennas & Propag. Mag.* **55** 29

[3] Al-Joumayly M A and Behdad N 2011 *IEEE Trans. Antennas Propag.* **59** 4542

[4] Rahmati B and Hassani H R 2014 *IEEE Trans. Antennas Propag.* **63** 174

[5] Ryan C G M, Chaharmir M R, Shaker J, Bray J R, Antar Y M M and Ittipiboon A 2010 *IEEE Trans. Antennas Propag.* **58** 1486

[6] Wu R Y, Li Y B, Wu W, Shi C B and Cui T J 2017 *IEEE Trans. Antennas Propag.* **65** 3481

[7] Xu H X, Tang S, Wang G M, Cai T, Huang W, He Q, Sun S and Zhou L 2016 *IEEE Trans Antennas Propag* **64** 3676

[8] Wang Z B, Xue M, Zhang H, Wu Z and Li B 2016 *Int. J. RF. Microwave Comput. Aided Eng.* **26** 449

[9] Zhengbin W, Haofang W, Zhuangli D, Zhihang W, Yerong Z and Zhipeng Z 2017 *J. Chin. Universities Posts Tele.* **24** 10

[10] Pfeiffer C, Emani N K, Shaltout A M, Boltasseva A, Shalaev V M and Grbic A 2014 *Nano Lett.* **14** 2491

[11] Abdelrahman A H, Elsherbeni A Z and Yang F 2014 *IEEE Antennas Wireless Propag. Lett.* **13** 177

[12] Li H P, Wang G M, Liang J G, Gao X J, Hou H and Jia X 2017 *IEEE Trans. Antennas Propag.* **65** 1452

[13] Abdelrahman A H, Elsherbeni A Z and Yang F 2014 *IEEE Trans. Antennas Propag.* **62** 690

[14] Liu W, Chen Z N and Qing X 2014 *IEEE Trans. Antennas Propag.* **62** 1165

[15] Hecht E 2002 *Optics* (4th Edn.) (San Francisco: Addison Wesley)

[16] Nayeri P, Yang F and Elsherbeni A Z 2010 *IEEE Antennas Wireless Propag. Lett.* **9** 1139

[17] https://altairhyperworks.com.cn/product/FEKO

[18] Pham K, Nguyen N T, Clemente A, Palma L D, Coq L L, Dussopt L and Sauleau R 2016 *IEEE Trans. Antennas Propag.* **64** 2022

[19] Tian C, Jiao Y C and Zhao G 2016 *IEEE Antennas Wireless Propag. Lett.* **16** 465

[20] Li T J, Liang J G, Li H P and Liu Y Q 2016 *Chin. Phys. B* **25** 094101